



## Numerical simulation of the vibratory and impact installation of monopiles in saturated sand

Halvard Eiesland<sup>i)</sup>, Gudmund R. Eiksund<sup>ii)</sup>, Steven M. Bayton<sup>iii)</sup> and Jörgen Johansson<sup>iv)</sup>

i) MSc, Multiconsult Norge AS, Oslo, Norway.

ii) Professor, Dept. of Civil & Environmental Eng., Norwegian University of Science & Technology (NTNU), Trondheim, Norway.

iii) Ph.D., Norwegian Geotechnical Institute, Oslo Norway.

iv) Ph.D., Norwegian Geotechnical Institute, Oslo Norway.

### ABSTRACT

Offshore monopile installation by vibratory driving is proposed to have numerous operational and environmental advantages over traditional impact driving. That said, the uptake of this method has been rare, namely due to uncertainties related to pile bearing capacity after installation. This paper explores the numerical simulation of the soil response for a small portion of both vibro- and impact installation phases. Results indicate that for the same penetration depth achieved, the final stress state for both methods is similar. This may suggest that bearing capacity is also quite similar. In addition, the effect of different vibratory driving parameters and initial soil void ratio are also examined.

**Keywords:** vibratory, impact, installation, numerical simulation, monopile, sand

## 1 INTRODUCTION

### 1.1 Background

Offshore wind energy is positioning itself as an important player in the global transition from traditional fossil fuel to future renewable electricity generation. Indeed, the outlook for offshore wind in Europe is extensive, with the European Commission (EC) anticipating an increase of the offshore wind capacity of Europe from 12 GW to 300 GW by 2050 (EC, 2020).

Offshore wind turbines (OWT) are most commonly founded on monopile foundations. Despite increasing turbine size and progressively greater water depths, the share of monopile foundations continues to remain high; in 2020, 80 percent of the total number of installed OWTs was founded on monopiles (WindEurope, 2021). Monopiles are traditionally installed using impact hammers, whereby a ram repetitively impacts the pile head until the desired design penetration depth is reached.

### 1.2 Motivation

As the diameter of the monopile increases to accommodate the larger lateral loads and overturning moments, the impact installation method becomes increasingly challenging. Very large hammers are required to ensure full penetration, and this leads to a number of issues, not least the emission of substantial underwater noise causing harm to marine wildlife (Madsen et al., 2006). Vibratory pile driving is suggested to have several advantages compared to impact driving,

e.g. considerably less underwater noise emission and a faster installation time in certain soil conditions (Starre and Boor, 2011). That said, vibratory driving has rarely been applied to offshore applications, partly due to the uncertainty of final pile bearing capacity. Of the times that it has been adopted, pile load testing after installation, or final depth driving with an impact hammer to obtain end of driving data, have been considered necessary to estimate its bearing capacity. These both provide additional barriers to the uptake of vibratory pile installation.

With this in mind, better understanding of the soil response during vibratory driving may allow for better estimation of pile bearing capacity after installation, and ultimately lead to a greater utilisation of this pile installation method.

### 1.3 Objectives and approach

This paper presents a conceptual study of the soil response, both during and after, impact and vibratory driving of a monopile in a fully saturated sand. The objective is to investigate the difference in the simulated soil response subject to the two installation methods. The effect of different vibratory driving parameters and initial soil void ratio are also included.

For each installation method, a short period of the pile driving process is numerically simulated by the Finite Element Analysis (FEA) method using the software PLAXIS 2D. Both soil response and pile

vertical displacement during driving and after consolidation are presented.

#### 1.4 Impact vs. vibratory: driving principles

The principle of the impact hammer is to drive the pile into the soil by applying repetitive blows from a moving ram to the pile head, typically at a rate of 40-60 blows per min. Vibro-hammers generally apply a load of lower amplitude compared to impact hammers, but at a higher frequency. The principle of this installation method is to reduce the resistance of the soil by cyclic degradation. In saturated sands, the rapid cyclic movement may lead to build-up of excess pore pressure, contributing to a reduction of soil resistance.

The vertical vibratory force is the result of a centrifugal force from counter-rotating masses within the driver to cancel out horizontal force components. The resulting vertical force component  $F_{v,vib}(t)$  is described by the sinusoidal function (Holeyman, 2002):

$$F_{v,vib}(t) = M_{ecc} \cdot \omega^2 \cdot \sin(\omega \cdot t) \quad (1)$$

where  $M_{ecc}$  is eccentric moment of all rotating masses in the driver,  $\omega$  is the angular frequency and  $t$  is time.

## 2 NUMERICAL SIMULATION

The impact and vibratory pile driving processes are simulated in PLAXIS 2D. The model is axisymmetric about the vertical axis and the soil and pile are modelled by 15-noded triangle volume elements. The model space ranges from 0 m to 20 m in x-direction and from -45 m to 22 m in y-direction. Seabed is modelled at  $y = 0$  m, and sea level at  $y = 15$  m. Fig. 1(a) visualises the upper part of the axisymmetric model in PLAXIS 2D.

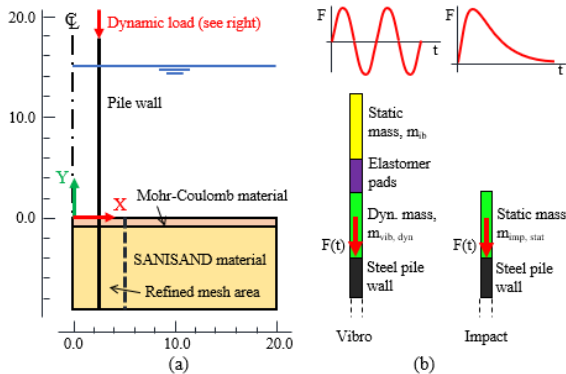


Fig. 1(a): Visualisation of upper part of PLAXIS 2D model; (b): Element clusters and dynamic load modelling the pile drivers.

The initial state of the monopile is wished-in-place to the final penetration depth. As such, only a small portion of the installation phase is simulated at the final penetration depth. A relatively low number of load cycles is then applied to the pile head.

Seven analysis cases are simulated, of which six replicate the vibratory driving process and one the impact driving process. Table 7 outlines the individual parameters adopted for the each of the seven cases.

### 2.1 Pile: material model and parameters

The monopile is an open-ended steel pile with an outer diameter ( $D_{outer, pile}$ ) equal to 5.0 m. The other pile dimensions are based on recommendations by API (2010) and Negro et al. (2017), which are related to pile outer diameter. The pile geometry is summarised in Table 1. A linear elastic material model is assigned to the modelled pile, with the parameters listed in Table 2.

Table 1. Pile geometry

Parameter	Symbol	Value	Unit
Outer pile diameter	$D_{outer, pile}$	5.0	m
Pile wall thickness	$t_{wall, pile}$	56.4	mm
Total pile length	$L_{total, pile}$	53.0	m
Driven pile length	$L_{embedded, pile}$	35.0	m
Embedment ratio	$L_{emb}/D_{outer}$	7.0	-

Table 2. Pile material properties

Parameter	Symbol	Value	Unit
Unsaturated specific weight	$\gamma_{pile, unsat}$	77	kN/m <sup>3</sup>
Elastic modulus	$E_{pile}$	$200 \cdot 10^6$	kN/m <sup>2</sup>
Poisson's ratio	$\nu_{pile}$	0.3	-

### 2.2 Soil: material model and parameters

The soil is modelled by the Simple Anisotropic Sand (SANISAND) constitutive model (Dafalias and Manzari, 2004). This material model incorporates isotropic and kinematic hardening. The latter is an important feature in simulations of soils subjected to cyclic loading since this also allows for the simulation of plastic strains at load reversals to previous stress states.

The SANISAND specific soil parameters in the simulations are adopted from Dafalias and Manzari (2004) which are obtained from a calibration on Toyoura sand. The parameters used are listed in Table 3.

Table 3. Soil (SANISAND) parameters (all unit-less) (Dafalias and Manzari, 2004)

Description	Symbol	Value
Elasticity	$G_0$	125
	$\nu$	0.05
Critical state	$M_c$	1.25
	$c$	0.712
	$\lambda_c$	0.019
	$e_0$	0.934
	$\xi$	0.7
Yield surface	$m$	0.01
	$h_0$	7.05
Plastic modulus	$Ch$	0.968
	$n^b$	1.1
	$A_0$	0.704
Dilatancy	$n^d$	3.5
	$Z_{max}$	5
Fabric-dilatancy tensor	$c_z$	600

In addition, the user-defined soil model of SANISAND requires input of atmospheric pressure  $p_{atm}$ , bulk modulus of the pore water  $K_w$ , shift of mean stress  $p_{mult}$  and initial void ratio  $e_{init}$ . These are set as  $p_{atm} = 101.3$  kPa,  $K_w = 0$ ,  $p_{mult} = 0$  and  $e_{init} = 0.734$ . The latter

representative of a sand with relative density ( $D_r$ ) of 66%, with  $e_{\min} = 0.61$  and  $e_{\max} = 0.97$  (Zhang, 2010). Note that  $K_w = 0$  is due to performing simulations in a drained state with consolidation (Mašín, 2015) and does not serve as input for the bulk modulus of the pore water.

The saturated specific weight of the sand is set to 20 kN/m<sup>3</sup>. Rayleigh damping is implemented to the soil material to simulate damping of elastic strains. See e.g. PLAXIS 2D (2020). The input values of Rayleigh damping alpha and beta coefficients depend on the frequency of the load replicating the pile driving. These are determined by selecting target frequencies of the damping at 5 Hz both above and below the frequencies of the applied load on the pile. The corresponding damping ratios are both set to 6%. The Rayleigh damping coefficients are listed in Table 7.

The soil is set drained with permeability parameters  $k_x = k_y = 1.5$  m/day. The coefficient of soil pressure at rest is set to  $K_{0,x} = K_{0,z} = 0.48$ , based on Jaky (PLAXIS 2D, 2020), with a friction angle obtained by the critical state line in triaxial compression and extension.

To avoid numerical instabilities due to zero stresses at seabed, the upper 1 m of the soil is modelled by the Mohr-Coulomb (MC) material model with an assigned value of cohesion greater than zero. The material properties of the MC soil are equal to the SANISAND soil, with Table 4 outlining any MC specific parameters.

Table 4. Soil (Mohr-Coulomb) parameters

Parameter	Symbol	Value	Unit
Effective elastic modulus	$E'$	$25 \cdot 10^3$	kN/m <sup>2</sup>
Effective Poisson's ratio	$\nu'$	0.25	-
Effective reference cohesion	$c'_{\text{ref}}$	1.0	kN/m <sup>2</sup>
Effective friction angle	$\phi'$	31.3	°
Dilatancy angle	$\psi$	0.0	°

### 2.3 Modelling of vibro-hammer

The hammer components, of both vibratory and impact driving, are modelled by element clusters on top of the pile and of same width as the pile wall thickness.

Table 5. Material parameters of vibro-hammer

Description	Mass [kg]	Elastic modulus [kN/m <sup>2</sup> ]
Dynamic mass ( $m_{\text{vib, dyn}}$ )	56640	$200 \cdot 10^6$
Static mass ( $m_{\text{ib}}$ )	15000	$200 \cdot 10^6$
Elastomer pads (spring)	0	1680

The element clusters modelling the components of the vibratory hammer – static and dynamic masses either side of elastomer pads (see Fig. 1(b)) – are assigned linear elastic material models. The elastomer pads isolate the static mass from vibrations of the dynamic load and pile. Parameters equal to the steel pile are assigned to these, with exception of the parameters listed in Table 5.

The load replicating the vibratory driving is assigned at the top of the steel pile, i.e. at the bottom of the dynamic mass,  $m_{\text{vib, dyn}}$ , as an evenly distributed load acting vertically downwards. The load is modelled by a

load multiplier being a sinusoidal function with a specified amplitude and frequency (12, 18 and 23.3 Hz).

### 2.4 Modelling of impact hammer

For the modelling of the impact hammer, the elastomer pads are not activated and  $m_{\text{vib, dyn}}$  is replaced with  $m_{\text{imp, stat}}$ . As per the vibratory hammer, the element cluster modelling the static mass is assigned a linear elastic material model, with parameters listed in Table 6.

Table 6. Material parameters of impact hammer

Description	Mass [kg]	Elastic modulus [kN/m <sup>2</sup> ]
Static mass ( $m_{\text{imp, stat}}$ )	$125 \cdot 10^3$	$200 \cdot 10^6$

Each impact load is modelled by a half sinusoidal curve with a frequency of 50 Hz and a determined load amplitude. One impact is modelled approximately every 2 seconds, giving a blow rate of 30 blows per minute.

### 2.5 Calculation parameters and phases

Details of the seven FEA simulations are presented in Table 7. After the initial soil stress calculation and wished-in-place pile setup, the pile is subjected to a dynamic load phase by the “Dynamic with consolidation” calculation type. For the vibratory driving simulations, 40 calculation steps are set per loading cycle. For the impact driving simulation, 8 calculation steps are performed each impact. This is followed by a dynamic damping phase, which partly damps out vibrations before consolidation phase is initiated. The excess pore pressures are allowed to dissipate to a value of 1.0 kPa during the consolidation phase.

## 3 RESULTS AND DISCUSSION

Compression stresses and strains are presented forthwith by negative values. The following results compare soil and pile response both during and after vibratory and impact driving processes.

### 3.1 Vibratory vs. impact driving

Simulations sim.A\* and sim.F are first chosen for presentation since these two show very similar final displacements after driving and consolidation (see Fig. 2), allowing for a more representative comparison of internal soil behaviour.

Fig. 3 presents the time history of mean effective stress at half embedment close to the exterior pile wall. Although the path toward the final value after consolidation is considerably different, it is seen to reach a very similar magnitude for both installation methods. Note the generally larger reduction in mean effective stress during vibratory driving, indicating a closer approach to soil liquefaction.

Excess pore pressure can be seen to increase considerably faster during vibratory driving, compared to impact driving (Fig. 4). The continuous vibro-loading appears to show no opportunity for excess pore pressure dissipation between load cycles. For impact installation,

Table 7. FEA simulation parameters

Description	Vibratory driving						Impact driving
	sim.A	sim.A*	sim.B	sim.C	sim.D	sim.E	sim.F
Reference	sim.A	sim.A*	sim.B	sim.C	sim.D	sim.E	sim.F
Driving frequency, $f$ [Hz]	23.3	23.3	18	12	12	23.3	-
Blow rate [blow/min.]	-	-	-	-	-	-	30
Dynamic time interval [s]	0.857	1.67	1.11	1.67	1.67	0.857	12.0
Number of cycles/impacts	20	38.9	20	20	20	20	7
Stress amplitude, $\sigma_v^A$ [kN/m <sup>2</sup> ]	10 609	10 609	6 315	2 807	10 609	10 609	101 315
Initial void ratio, $e_{init}$ [-]	0.734	0.734	0.734	0.734	0.734	0.650	0.734
Rayleigh damping of soil ( $\alpha$ )	8.391	8.391	6.262	3.738	3.738	8.391	18.66
Rayleigh damping of soil ( $\beta$ ) ( $\cdot 10^{-3}$ )	0.4093	0.4093	0.5305	0.7958	0.7958	0.4093	0.1910

on the other hand, despite a very sharp increase (and immediate decrease) of excess pore pressure at each blow, a minor dissipation is observed between impacts, resulting in a lower overall generation of excess pore pressure compared to the vibratory installation.

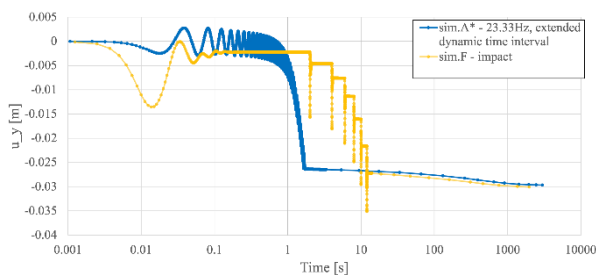


Fig. 2. sim.A\* (vibro, blue) and sim.F (impact, yellow): vertical displacement ( $u_y$ ) of top of pile during loading, damping and consolidation phases on a logarithmic time scale.

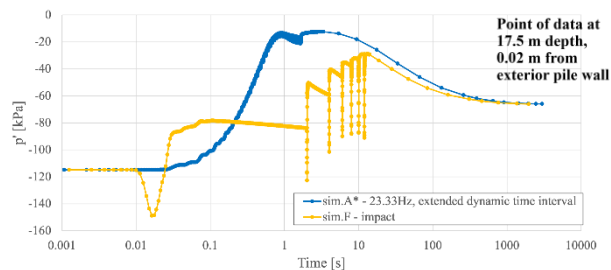


Fig. 3. sim.A\* (vibro, blue) and sim.F (impact, yellow): mean effective stress ( $p'$ ) during loading, damping and consolidation phases on a logarithmic time scale.

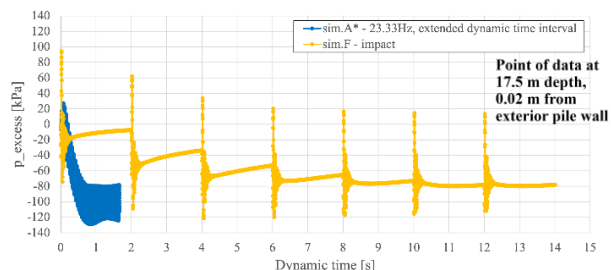


Fig. 4. sim.A\* (vibro, blue) and sim.F (impact, yellow): excess pore pressure ( $p_{excess}$ ) during loading phase (damping phase included for sim.F) against the dynamic time.

Note that the number of simulated loading cycles are relatively few compared to a full installation and the evolution of  $p_{excess}$  for further loading is not captured.

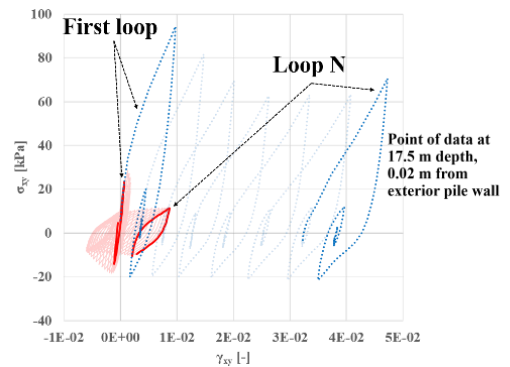


Fig. 5. sim.A\* (vibro, red line) and sim.F (impact, blue dotted line):  $\sigma_{xy}$ - $\gamma_{xy}$  hysteresis loops during loading phase (damping phase included for sim.F). First and last loop are emphasised.

Fig. 5 shows the  $\sigma_{xy}$ - $\gamma_{xy}$  hysteresis loops. The slope of the loops may be interpreted as the shear modulus, and it can be seen that vibratory driving exhibits a greater reduction of shear modulus at the end of installation. This is clearly illustrated by the calculated secant shear modulus ratio from cycle 1 to N ( $G_{s,N}/G_{s,1}$ ) estimated to be 0.13 and 0.54 for sim.A\* and sim.F respectively.

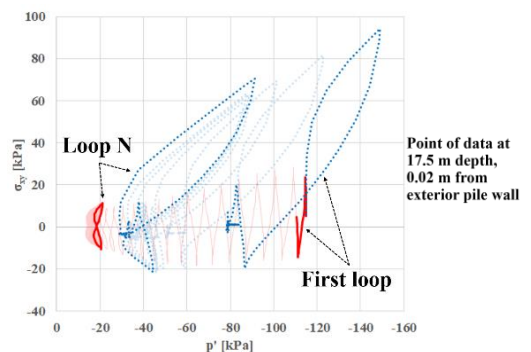


Fig. 6. sim.A\* (vibro, red line) and sim.F (impact, blue dotted line): stress path in  $p'$ - $\sigma_{xy}$  space during loading phase (damping phase included for sim.F). First and last loop are emphasised.

Fig. 6 shows the stress path in  $p'$ - $\sigma_{xy}$  space. Cyclic mobility is observed immediately during the first loading cycle of impact driving, indicated by the increased  $p'$  in compression within one cycle. This suggests an increase of driving resistance of the soil. It is likely that some of the energy generated by the driver is dissipated into plastic deformations leading to this increased driving



resistance. For the vibratory case, mean effective stress is almost solely decreasing and cyclic mobility is seen to a lesser degree and not until after several loading cycles. The mean effective stress may in fact decrease to such a degree that the pile settle solely due to its self-weight.

**3.2 Vibro: effect of lower driving frequency with associated smaller load amplitude**

A study into the vibratory load frequency is made. The driving frequency is lowered, and as such the vertical load amplitude is lowered accordingly, based on the relation presented in Eq. 1.

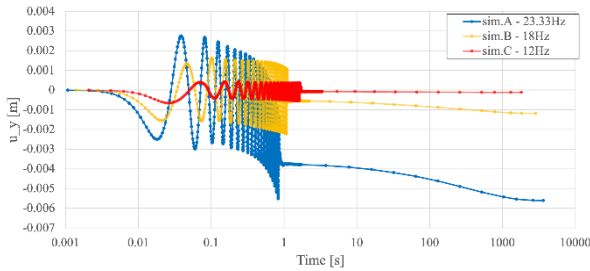


Fig. 7. sim.A (blue), sim.B (yellow) and sim.C (red): vertical displacement ( $u_y$ ) of top of pile during loading, damping and consolidation phases on a logarithmic time scale.

Vertical displacement of the pile head is plotted in Fig. 7. This indicates a close to zero pile penetration during driving at 12 Hz and a very small magnitude of penetration at 18 Hz. These results may therefore suggest that the threshold of pile penetration for these particular simulations lies between these two driving frequencies. Vertical displacement is considerably greater during driving at 23.3 Hz and suggests a non-linear relation between driving frequency, with associated load amplitude, and vertical pile displacement.

The higher frequency installation is seen to result in a more rapid increase of excess pore pressure (Fig. 8). Driving at 12 Hz shows almost no noticeable build-up of excess pore pressure.

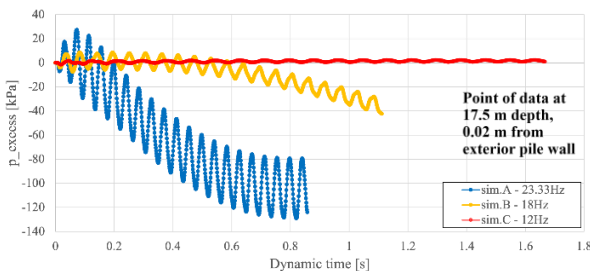


Fig. 8. sim.A (blue), sim.B (yellow) and sim.C (red): excess pore pressure ( $p_{excess}$ ) during loading phase against the dynamic time.

Given the coupled physical effect of lower load magnitude with lower vibration frequency (Eq. 1), it is not fully clear which parameter governs the observed soil responses. An independent study into load frequency, with similar amplitude is therefore conducted.

**3.3 Vibro: effect of lower driving frequency with similar load amplitude**

Results of vibratory driving at 23.3 Hz and 12 Hz, with similar load amplitudes, are now compared to independently evaluate the effect of loading rate.

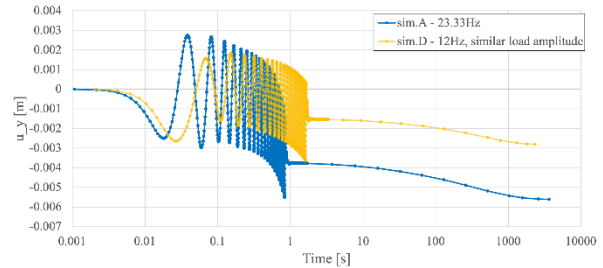


Fig. 9. sim.A (blue) and sim.D (yellow): vertical displacement ( $u_y$ ) of top of pile during loading, damping and consolidation phases on a logarithmic time scale.

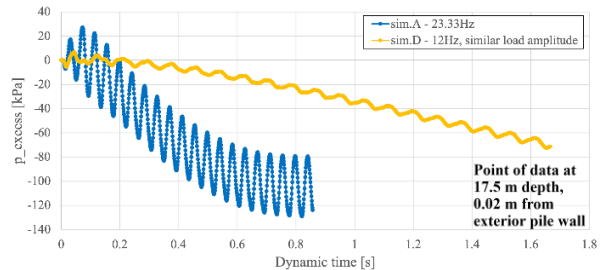


Fig. 10. sim.A (blue) and sim.D (yellow): excess pore pressure ( $p_{excess}$ ) during loading phase against the dynamic time.

Fig. 9 shows the vertical displacement of the pile head during 20 cycles at 23.3 Hz and 12 Hz, and the following consolidation, where the final displacement is seen to be greater for the higher load frequency. Note that the final pile displacement is considerably higher for sim.D (yellow line in Fig. 9) compared to sim.C (red line in Fig. 7), of which the load frequencies are the same, but the latter subject to a lower load amplitude. The higher rate of shearing of the soil is also seen to give a more rapid build-up of excess pore pressure (Fig. 10), which seems to approach a steady-state after the 20 cycles. For the lower load frequency, this steady-state is not yet reached for the same number of 20 cycles.

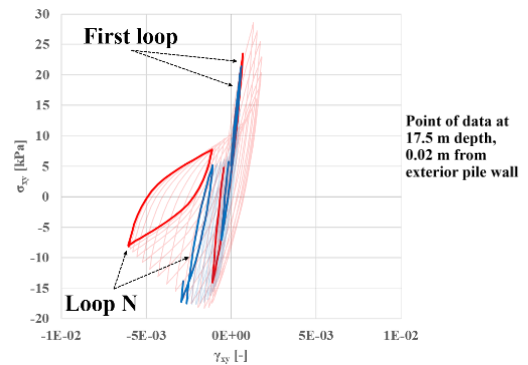


Fig. 11. sim.A (red line) and sim.D (blue line):  $\sigma_{xy}$ - $\gamma_{xy}$  hysteresis loops during loading phase. First and last loop are emphasised.

The hysteresis loops in Fig. 11 emphasise the effect of an increased driving frequency. The higher frequency clearly leads to greater cyclic degradation. The load amplitude and frequency of sim.D may therefore be insufficient to allow cyclic degradation.

### 3.4 Vibro: effect of initial void ratio

Finally, the effect of initial void ratio of the sand, i.e. density, on pile driving is investigated. Simulations sim.A and sim.E have initial void ratios of 0.734 (medium dense) and 0.650 (very dense) respectively.

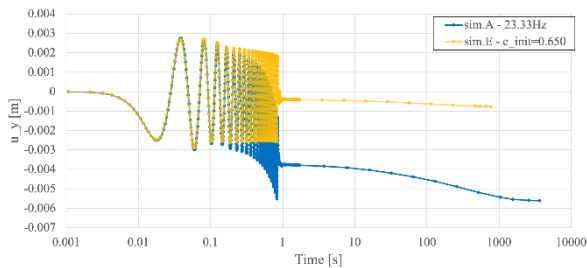


Fig. 12. sim.A (blue) and sim.E (yellow): vertical displacement ( $u_y$ ) of top of pile during loading, damping and consolidation phases on a logarithmic time scale.

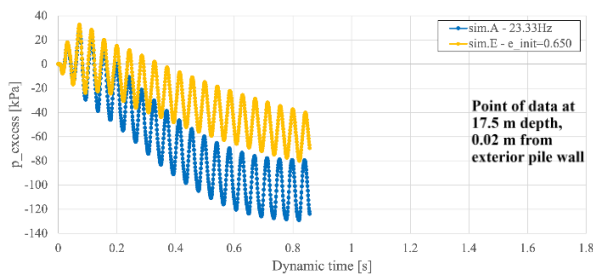


Fig. 13. sim.A (blue) and sim.E (yellow): excess pore pressure ( $P_{\text{excess}}$ ) during loading phase against the dynamic time.

Fig. 12 shows a considerably higher rate of vertical displacement during driving and after consolidation for the soil of lower relative density (sim.A). The evolution of excess pore pressure also builds at a higher rate during driving for the initially looser soil (Fig. 13). This indicates that vibratory driving is significantly more effective in looser sands.

## 4 CONCLUSIONS

This paper presents results from simulations of pile installations for both impact and vibratory driving. The results show a close to similar stress state of the soil after consolidation following the driving for the two methods, regardless of the different stress paths during driving. This may indicate a similar bearing capacity of these two piles. The presented modelling approach is believed to be a valuable contribution to investigate the differences in soil response during driving for the two methods, and ultimately the pile bearing capacity of vibro-installed piles.

The study also show that for vibratory driving the pile penetration rate are affected by both the amplitude and

the frequency of the cyclic loading. Larger load amplitude and increased frequency both lead to faster excess pore pressure build-up and increased pile penetration.

In order to validate the numerical results observed in this study, comparison to model and/or field scale testing observations is important.

## ACKNOWLEDGEMENTS

The first author expresses gratitude towards Multiconsult for enabling the writing of the paper and to colleagues for their support and knowledge sharing.

## REFERENCES

Reference is made to Eiesland (2021) for a more detailed review of the content in the present paper.

- [1] API (2010). "Recommended Practice for Planning, Designing and Constructing Fixed Off-shore Platforms – Working Stress Design". (RP 2A-WSD) Twenty-first edition. American Petroleum Institute (API)
- [2] Dafalias, Y. F. and Manzari, M. T. (2004). "Simple Plasticity Sand Model Accounting for Fabric Change Effects", *Journal of Engineering Mechanics*, 130(6), American Society of Civil Engineers, pp. 622-634.
- [3] EC (2020). "Boosting Offshore Renewable Energy for a Climate Neutral Europe". European Commission. URL: [https://ec.europa.eu/commission/presscorner/detail/en/IP\\_20\\_2096](https://ec.europa.eu/commission/presscorner/detail/en/IP_20_2096) (visited on 16<sup>th</sup> April 2021).
- [4] Eiesland, H. (2021). "Numerical Simulation of Monopile Vibratory and Impact Installation in Saturated Sand", Master's thesis at Norwegian University of Science and Technology (NTNU).
- [5] Holeyman, A. E. (2002). "Soil Behaviour under Vibratory Driving". *Proceedings of the International Conference on Vibratory Pile Driving and Deep Soil Compaction - TRANSVIB2002*, Belgium.
- [6] Madsen, P. T. et al. (2006). "Wind turbine underwater noise and marine mammals: implications of current knowledge and data needs". *Marine Ecology Progress Series*, 309, pp. 279-295.
- [7] Mašin, D. (2015). "Implementation of SANISAND model as ABAQUS umat and PLAXIS user defined subroutines". README document.
- [8] Negro, V. et al. (2017). "Monopiles in offshore wind: Preliminary estimate of main dimensions". *Ocean Engineering*, 133, pp. 253-261
- [9] PLAXIS 2D – General Information Manual (2021). V21.01.
- [10] PLAXIS 2D – Reference Manual (2020). V20.04.
- [11] Starre, H. V. and Boor, J. (2011) (interview) "Vibratory Hammers". Saleem, Z., interviewer. Reference to interview is made in "Alternatives and modifications of Monopile foundation or its installation technique for noise mitigation" by Saleem, Z. (2011).
- [12] WindEurope (2021). "Offshore Wind in Europe – key trends and statistics 2020". URL <https://windeurope.org/data-and-analysis/product/o> (visited on 22<sup>nd</sup> February 2021). shore-wind- in-europe-key-trends-and-statistics-2020.
- [13] Zhang, F. et al. (2010). "A Try to Give a Unified Description of Toyoura Sand". *Soils and Foundations*, 50.5, pp. 679-693. Japanese Geotechnical Society.